JOURNAL OF THERMOPHYSICS AND HEAT TRANSFER
Vol. 17, No. 4, October–December 2003

Three-Dimensional Gravity-Jitter Induced Melt Flow and Solidification in Magnetic Fields

K. Li* and B. Q. Li†
Washington State University, Pullman, Washington 99163
and
H. C. de Groh‡
NASA John H. Glenn Research Center, at Lewis Field, Cleveland, Ohio 44135

A full three-dimensional transient numerical model is presented for gravity- (*g*-) jitter induced melt flow and solidification phenomena with and without externally applied magnetic fields during the melt growth of Sn-doped Bi single crystals in microgravity. The model is developed based on a Eulerian–Lagrangian finite element formulation, coupled with a mesh-deforming algorithm to track the solidification front. Extensive numerical simulations are carried out, and the studied parameters include solute concentration-dependent melting temperature, solidification interface morphology, magnetic field direction and magnitude, idealized microgravity condition, and synthesized and real *g*-jitter data conditions. Computed results show that *g*-jitter induced melt flow is time dependent and exhibits a complex three-dimensional structure and that the flow can have detrimental effects on solute concentration distribution. The *g*-jitter induced melt flow and its deleterious effects on solidification can be suppressed by externally applied magnetic fields. The three-dimensional numerical simulations suggest that a two-dimensional model is useful in providing some essential features of *g*-jitter induced flow and solidification behavior with and without externally applied magnetic fields and that a three-dimensional model is required to resolve fully the complex spatial flow structure when all *g*-jitter components are operative during a realistic space flight.

Nomenclature

$\boldsymbol{A}(\boldsymbol{U})$	=	advection stiffness matrix
$\boldsymbol{B}$	=	gradient matrix
B_0	=	magnetic field magnitude
C	=	dimensionless concentration
$\boldsymbol{C}$	=	global nodal concentration vector
C_p	=	specific heat of Sn
C_0	=	solute concentration of the inflow
D	=	solute diffusivity
$\mathrm{d}T/\mathrm{d}x$	=	temperature gradient
$\boldsymbol{F}$	=	force vector
Gr_S	=	solutal Grashof number
Gr_T	=	thermal Grashof number
$\boldsymbol{g}_n$	=	dimensionless amplitude of the single-frequency gravity- (g-) jitter
$\boldsymbol{g}(t)$	=	dimensionless real g-jitter
g_0	=	terrestrial gravity level
H	=	latent heat of Sn
Ha	=	Hartmann number
$h(z)$	=	dimensionless interface z coordinate
$\hat{\boldsymbol{i}}, \hat{\boldsymbol{j}}$	=	unit vector of ith and jth component
$\boldsymbol{K}$	=	diffusion stiffness matrix
k	=	thermal conductivity
k_0	=	solute segregation coefficient
L_c	=	length of cold zone
L_g	=	length of gradient zone
L_h	=	length of hot zone
L_0	=	dimensionless length of ampoule
$\boldsymbol{M}$	=	mass matrix
m	=	slope of solidus curve
$\hat{n}$	=	unit normal vector
Pr	=	Prandtl number
p	=	dimensionless pressure
p_0	=	pressure scale
Ra	=	radiation number of ampoule
R_0	=	length scale
Sc	=	Schmidt number
Ste	=	Stefan number
T	=	dimensionless temperature
$\boldsymbol{T}$	=	global nodal temperature vector
T_c	=	cold zone temperature
T_h	=	hot zone temperature
T_m	=	dimensionless melting temperature
T^*	=	temperature
t_0	=	timescale
$\boldsymbol{U}$	=	global velocity vector containing all of the nodal values
U_0	=	velocity scale
$\vec{\boldsymbol{U}}$	=	dimensionless velocity vector
$\vec{\boldsymbol{U}}^*$	=	dimensionless interface velocity
u	=	dimensionless x direction velocity
V_g	=	crystal pulling velocity
V_p	=	dimensionless crystal pulling velocity
v	=	dimensionless y direction velocity
W_i	=	inner diameter of ampoule
W_i^*	=	dimensionless inner diameter of ampoule
W_o	=	outer diameter of ampoule
W_o^*	=	dimensionless outer diameter of ampoule
w	=	dimensionless z direction velocity
β_C	=	solutal expansion coefficient
β_T	=	thermal expansion coefficient
ΔT	=	temperature scale
$\partial\Omega$	=	computational domain boundary
ε	=	penalty parameter for pressure
$\varepsilon_{\mathrm{amp}}$	=	radiation coefficient of ampoule
κ	=	thermal diffusivity
ν	=	kinematic viscosity
ρ_0	=	density of pure Sn at T_m

Received 31 January 2003; accepted for publication 24 April 2003.

*Research Associate, School of Mechanical and Materials Engineering.
†Professor, School of Mechanical and Materials Engineering; li@mme.wsu.edu.
‡Senior Scientist.

σ_m = electrical conductivity
Φ = electric potential
$\mathbf{\Phi}$ = global nodal electric potential vector
Ω = computational domain
ω_n = frequency of the single-frequency g-jitter

Subscripts

amb = ambient
amp = ampoule
C = coefficient relative to concentration
cry = crystal
i, j = ith, jth component
p = coefficient relative to penalty continuity
T = coefficient relative to temperature
U = coefficient relative to velocity

Superscipt

T = matrix transpose

I. Introduction

THE essential reason to go to space for melt growth of single crystals lies in a promise that a substantial reduction of gravity level achieved in spacecraft may result in a quiescent melt pool, thereby allowing a diffusion-controlled growth condition to be realized. Indeed, in some of the early growth experiments with certain materials, the promise has been fulfilled during a short duration of space flight. More recent space experiments on the melt growth of single crystals, however, have repeatedly shown that qualities of space growth crystals are largely irreproducible over a longer duration of a space flight. It is now understood that this problem is caused by the melt convective flow induced by residual gravity (g) perturbations, namely, g-jitter. Although orders of magnitudes smaller than gravity on earth, g-jitter induced convection still is sufficiently intense that it overshadows the growth mechanism by pure diffusion. Analysis of space grown crystals indicates that g-jitter forces represent deviations from a dynamic weightlessness condition created in spacecraft such as space shuttles and the International Space Station being constructed. A variety of sources may contribute to the occurrence of g-jitter, which include atmospheric drag, solar radiation, thruster firings, pump and other mechanical component operations, and astronaut exercises.[1] Figure 1 shows the characteristics of g-jitter signals recorded by onboard accelerometers during a space flight. Evidently, g-jitter is intrinsically three-dimensional in nature and is random both spatially and temporally.

Many studies have appeared on the subject of g-jitter and its effects on melt flows in crystal growth systems.[2–6] Numerical results have demonstrated that the frequency, amplitude, and spatial orientation of g-jitter all play important roles in the melt flows. The most detrimental effects of g-jitter come from the low-frequency components with large amplitudes, especially when they are aligned perpendicularly with the temperature gradient, which usually is the crystal growth direction.[2,3] However, most studies published so far have neglected the solidification phenomena by assuming a flat solidification interface. An exception is the recent work by Benjapiyaporn et al.[7] and Timchenko et al.,[8] who studied the interface morphology in a two-dimensional numerical model of a Bridgman–Stockbarger space crystal growth system. Their research suggests that the solidification interface shape deviates from the flat interface assumption and that for the accurate prediction of solidification interface morphology, the solute dependency of the melting temperature should be accounted for, although their studies did not consider such dependency.

Magnetic damping has been widely used for crystal quality control under terrestrial conditions,[9] and its application to suppress the low-frequency g-jitter induced flows in microgravity environment has been explored recently.[10–18] Both analytical and numerical methods have been applied including a two-dimensional model developed to represent the crystal growth system under the combined action of g-jitter and magnetic fields.[10–18] Although the two-dimensional model is very valuable in providing a basic understanding of g-jitter induced melt flow and its effects on solidification, its limitation is evident, especially in light of the three-dimensional nature of driving g-jitter forces. Thus, a full three-dimensional model is required to understand the complex, time-dependent, three-dimensional g-jitter induced melt flow and transport phenomena and their interaction with an applied magnetic field. Also, a three-dimensional model should be useful in fully assessing the validity and limitation of the previously developed two-dimensional models. Such a full three-dimensional modeling study, to the best of the authors' knowledge, appears to have not yet been carried out.

This paper presents a full three-dimensional transient numerical model for the g-jitter induced melt flow, heat and solute transport, solidification interface morphology, and induced electromagnetic field distribution in a crystal growth system planned for space flight experiments. The model development is based on the finite element solution to the transient, three-dimensional Navier–Stokes equations, thermal and solute transport equations, and the magnetodynamic forms of the Maxwell equations under both idealized and realistic g-jitter conditions. In modeling the transient three-dimensional convection and the moving interface evolution as affected by internal convection, a Eulerian–Lagrangian formulation has been applied to reformulate the problem in moving coordinates, and a front-tracking finite element method is employed to obtain the required numerical accuracy and sensitivity for solidification interface morphology. The model also includes the double diffusive effects and allows for a full account of the solute effects on the melting temperature. Such a comprehensive, complex three-dimensional magnetohydrodynamic model can be computationally extremely intensive and require substantial computing resources.

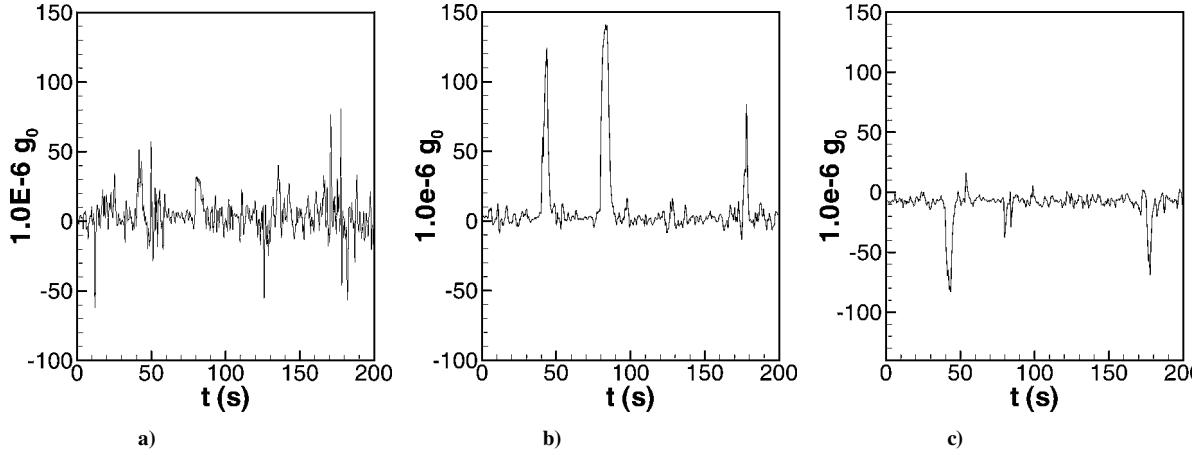

Fig. 1 ***G*-jitter signatures taken by an onboard accelerometer during a space flight: a) x direction, b) y direction, and c) z direction.**

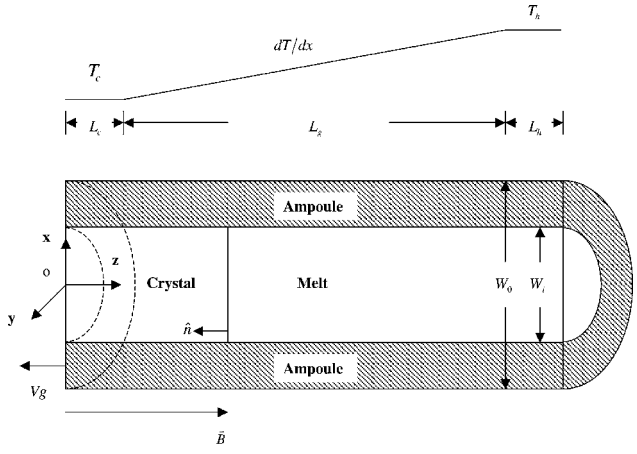

Fig. 2 Schematic representation of the *r–z* plane cut of the three-dimensional Bridgman–Stockbarger single crystal growth system in space.

To enhance the computational performance of the three-dimensional model, a physics-based renumbering algorithm for matrix elements has been developed. Numerical tests suggest that for the systems studied, an improvement of about two orders of magnitude in computational speed is achieved with the renumbering algorithm.[19] The three-dimensional modeling results also confirm that g-jitter induced flows in general are truly three-dimensional in space crystal growth systems. However, in the symmetry plane parallel to the direction of g-jitter, a two-dimensional model captures some of very essential features of g-jitter induced melt flow, and there it provides a reasonable representation of both melt flow and solute transport.

II. Problem Statement

Figure 2 schematically illustrates the three-dimensional cylindrical model for a Bridgman–Stockbarger furnace for the melt growth of Sn-doped Bi single crystals in a space flight, where $\boldsymbol{B}$ is the applied magnetic field. Its configuration is similar to that used for the MEPHISTO space flight experiments.[20] In space, the residual acceleration experienced by the spacecraft has both steady and time-dependent acceleration components (g-jitter), which are known to cause melt convection in the liquid pool. An external dc magnetic field is applied to suppress the detrimental convection effects induced by the g-jitter during crystal growth. For the purpose of illustration, a commonly used magnetic field configuration is shown in Fig. 2. The three-dimensional model to be presented, however, allows an arbitrary orientation of an external dc field in any directions. The time-dependent phenomena of melt flow, heat and mass transfer, and solidification in the system are described by the full three-dimensional transient magnetohydrodynamic equations and the thermal and solute transport equations, along with the liquid–solid interface energy balance equation for the interface morphology. For the crystal growth applications under consideration, the magnetic Reynolds number is small.[12] Thus, the induced magnetic field is negligible in comparison with the imposed magnetic field, and the time variation of the induced electric field may also be neglected.[21] With these considerations, the Maxwell equations are simplified to one scalar transport equation for the electric potential. Note that, for a two-dimensional model, the induced electric field is zero for an appropriate arrangement, and hence, the electric potential equation is trivially satisfied.[18] Thus the governing equations for the present three-dimensional studies are written in the nondimensional form as

$$\nabla \cdot \vec{\boldsymbol{U}} = 0 \tag{1}$$

$$\frac{\partial \vec{\boldsymbol{U}}}{\partial t} + \vec{\boldsymbol{U}} \cdot \nabla \vec{\boldsymbol{U}} = -\nabla p + \nabla^2 \vec{\boldsymbol{U}} + [-Gr_T(T - T_m) + Gr_S(C-1)]\boldsymbol{g}(t) + Ha^2(-\nabla\Phi + \vec{\boldsymbol{U}} \times \boldsymbol{B}) \times \boldsymbol{B} \tag{2}$$

$$\frac{\partial T}{\partial t} + \vec{\boldsymbol{U}} \cdot \nabla T = \frac{1}{Pr}\nabla^2 T \tag{3}$$

$$\frac{\partial C}{\partial t} + \vec{\boldsymbol{U}} \cdot \nabla C = \frac{1}{Sc}\nabla^2 C \tag{4}$$

$$\nabla^2 \Phi = \nabla \cdot (\boldsymbol{B} \times \vec{\boldsymbol{U}}) \tag{5}$$

$$\frac{\partial T_{\text{cry}}}{\partial t} + V_p(\hat{e}_z \cdot \nabla T_{\text{cry}}) = \frac{\kappa_{\text{cry}}}{\kappa}\frac{1}{Pr}\nabla^2 T_{\text{cry}} \tag{6}$$

$$\frac{\partial T_{\text{amp}}}{\partial t} + V_p(\hat{e}_z \cdot \nabla T_{\text{amp}}) = \frac{\kappa_{\text{amp}}}{\kappa}\frac{1}{Pr}\nabla^2 T_{\text{amp}} \tag{7}$$

where the standard Boussinesq assumption has been used to account for solute and temperature effects. Note that the last two equations describe the thermal field in the crystal and the ampoule. The solute diffusion in the solid is also neglected. In nondimensionalizing the preceding equations, the following scales have been used: $R_0 = 0.5W_i$ for length, $U_0 = \nu/R_0$ for velocity, $t_0 = R_0^2/\nu$ for time, $p_0 = \rho_0 U_0^2$ for pressure, C_0 for concentration, g_0 for gravity, B_0 for magnetic field, and $\Delta T = (T_h - T_c)$ for temperature, whereas the temperature is nondimensionialized by $(T^* - T_c)/\Delta T$. Note that instead of ν, thermal diffusivity may also be chosen to nondimensionalize the equations for this problem. The nondimensional parameters are defined as

$$Gr_T = \beta_T R_0^3 g_0 \Delta T \big/ \nu^2, \qquad Gr_S = \beta_c R_0^3 g_0 C_0 \big/ \nu^2, \qquad Pr = \nu/\kappa$$

$$Sc = \nu/D, \qquad Ra = \varepsilon_{\text{amp}} \sigma R_0 (\Delta T)^3 \big/ k_{\text{amp}}, \qquad V_p = V_g/U_0$$

$$Ste = H/\Delta T C_p, \qquad Ha = B_0 R_0 \sqrt{\sigma_m/\rho_0 \nu}, \qquad W_0^* = W_0/R_0$$

$$W_i^* = W_i/R_0, \qquad L_0^* = L_0/R_0$$

The boundary conditions represent the physical constraints of the system and are formulated as

$$T = 0, \qquad \text{at} \qquad z = 0 \tag{8}$$

$$T = 1, \qquad \text{at} \qquad z = L_0^* \tag{9}$$

$$\hat{n} \cdot \nabla T = -Ra\left[\left(T + T_c^*\right)^4 - \left(T_{\text{amb}} + T_c^*\right)^4\right] \qquad \text{at} \qquad 0 \le z \le L_0^*, \qquad r = W_0^* \tag{10}$$

$$\hat{n} \cdot \nabla T = (k_{\text{amp}}/k_{\text{cry}})(\hat{n} \cdot \nabla T_{\text{amp}}) \qquad \text{at} \qquad 0 \le z \le h(z), \qquad r = W_i^* \tag{11}$$

$$\hat{n} \cdot \nabla T = (k_{\text{amp}}/k)(\hat{n} \cdot \nabla T_{\text{amp}}) \qquad \text{at} \qquad h(z) \le z \le L_0^*, \qquad r = W_i^* \tag{12}$$

$$\hat{n} \cdot \vec{\boldsymbol{U}} = 0, \qquad \hat{n} \times \vec{\boldsymbol{U}} = V_p, \qquad \hat{n} \cdot \nabla C = 0 \qquad \text{at} \qquad h(z) \le z \le L_0^*, \qquad r = W_i^* \tag{13}$$

$$\hat{n} \cdot \vec{\boldsymbol{U}} = V_p, \qquad \hat{n} \times \vec{\boldsymbol{U}} = 0, \qquad \hat{n} \cdot \nabla C = V_p Sc(C-1) \qquad \text{at} \qquad z = L_0^*, \qquad 0 \le r \le W_i^* \tag{14}$$

$$\hat{n} \cdot (\vec{\boldsymbol{U}} - \vec{\boldsymbol{U}}^*) = \hat{n} \cdot \left(\vec{\boldsymbol{U}}_{\text{cry}} - \vec{\boldsymbol{U}}^*\right), \qquad \hat{n} \times (\vec{\boldsymbol{U}} - \vec{\boldsymbol{U}}_{\text{cry}}) = 0$$

$$\hat{n} \cdot \nabla C = Sc\left[\hat{n} \cdot (\vec{\boldsymbol{U}} - \vec{\boldsymbol{U}}^*)C - \hat{n} \cdot \left(\vec{\boldsymbol{U}}_{\text{cry}} - \vec{\boldsymbol{U}}^*\right)C_{\text{cry}}\right]$$

$$T = T_m + mC, \qquad \text{at} \qquad z = h(z), \qquad 0 \le r \le W_i^* \tag{15}$$

$$(\hat{n} \cdot \nabla T) - (k_{\text{cry}}/k)(\hat{n} \cdot \nabla T_{\text{cry}}) = Ste\,Pr\,\hat{n} \cdot \left(\vec{\boldsymbol{U}}_{\text{cry}} - \vec{\boldsymbol{U}}^*\right) \qquad \text{at} \qquad z = h(z), \qquad 0 \le r \le W_i^* \tag{16}$$

$$\hat{n} \cdot \nabla \Phi = 0, \qquad \text{at} \qquad z = 0, \qquad L_0^*, \qquad r = W_i^* \tag{17}$$

where $T_c^* = T_c/\Delta T$, $C_{\text{cry}} = k_0 C$, $\hat{n}\cdot\vec{U}_{\text{cry}} = V_p$, and $\hat{n}\times\vec{U}_{\text{cry}} = 0$. Note that Eq. (16) represents the thermal energy balance along the interface due to the latent heat release and along with the temperature continuity condition (15) determines the solidification interface position.

III. Finite Element Solution

The governing equations described in Sec. II, along with the boundary conditions, are solved using the deforming Galerkin finite element method. The formulations and relevant benchmark tests were detailed in previous publications for both two- and three-dimensional calculations,[14,16,18,22] and thus, only an outline is given here. Applying the standard finite element procedures to the preceding equations and carrying out involved algebraic operations, one has the following set of matrix equations for the unknowns defined at the nodal points:

$$\begin{bmatrix} \boldsymbol{M} & \boldsymbol{0} & \boldsymbol{0} & \boldsymbol{0} \\ \boldsymbol{0} & \boldsymbol{M}_T & \boldsymbol{0} & \boldsymbol{0} \\ \boldsymbol{0} & \boldsymbol{0} & \boldsymbol{M}_C & \boldsymbol{0} \\ \boldsymbol{0} & \boldsymbol{0} & \boldsymbol{0} & \boldsymbol{0} \end{bmatrix} \begin{bmatrix} \dot{\boldsymbol{U}} \\ \dot{\boldsymbol{T}} \\ \dot{\boldsymbol{C}} \\ \dot{\boldsymbol{\Phi}} \end{bmatrix} + \begin{bmatrix} \boldsymbol{A}_U(\boldsymbol{U}) + \boldsymbol{K}_U + \dfrac{1}{\varepsilon}\boldsymbol{E}\boldsymbol{M}_p^{-1}\boldsymbol{E}^T & \boldsymbol{B}_T & \boldsymbol{B}_C & \boldsymbol{B}_\Phi \\ \boldsymbol{0} & \boldsymbol{A}_T(\boldsymbol{U}) + \boldsymbol{K}_T & \boldsymbol{0} & \boldsymbol{0} \\ \boldsymbol{0} & \boldsymbol{0} & \boldsymbol{A}_C(\boldsymbol{U}) + \boldsymbol{K}_C & \boldsymbol{0} \\ \boldsymbol{D}_\Phi & \boldsymbol{0} & \boldsymbol{0} & \boldsymbol{K}_\Phi \end{bmatrix} \times \begin{bmatrix} \boldsymbol{U} \\ \boldsymbol{T} \\ \boldsymbol{C} \\ \boldsymbol{\Phi} \end{bmatrix} = \begin{bmatrix} \boldsymbol{F}_U \\ \boldsymbol{F}_T \\ \boldsymbol{F}_C \\ \boldsymbol{F}_\Phi \end{bmatrix} \tag{18}$$

Note that unlike the two-dimensional case, the three-dimensional model must include the electric potential as a variable because it is no longer a constant. The preceding matrix equations are solved using the successive substitution method, and the time derivatives are approximated using the implicit finite difference scheme.

Equation 18, as earlier formulated, represents an extremely computationally challenging task when the lower–upper (LU) decomposition method is used to invert the matrix, even with all necessary speed-improving measures such as skyline storage and an optimized heuristic renumbering scheme. Tests with a flat interface model using about 6000 nodes on a SGI supercomputer (six processor Onyx) machine showed that an iteration requires about 120 min to complete. A typical transient simulation requires about 1000 time steps, and within each step about 3–4 iterations are needed to converge. This means a complete run would require about one year CPU time. Examination of the matrix structure, however, suggests that the submatrices $\boldsymbol{D}$ and all $\boldsymbol{B}$ may be moved to the right side through simple matrix operations to reduce substantially the bandwidth of the final matrix. For a flow simulation where flow velocity is not high, such as the case being considered, matrices $\boldsymbol{B}_T$ and $\boldsymbol{B}_C$ may be put on the right-hand side with a decreased numerical performance. This physics-based rearranging, followed by renumbering the final matrix by regrouping $\boldsymbol{A}_T + \boldsymbol{K}_T$, $\boldsymbol{A}_C + \boldsymbol{K}_C$, and $\boldsymbol{K}_\Phi$ into three separate matrices, each stored in a skyline format, has greatly reduced computational burdens associated with the three-dimensional simulations. In fact, numerical tests show that a factor of about 120 in speed increase is achieved with this arrangement, compared with the traditional skyline-LU-based approach.[19]

To calculate the dynamic change of the moving interface, that is, the solidification front between the liquid and solid phases, a Eulerian–Lagrangian description is adopted, and finite elements are allowed to move to track the moving surface. Thus, a region that covers the solidifying liquid and solid is defined, and the nodes within the region are allowed to move in accordance with the interface movement. These additional velocities that result from the mesh movement are added to the velocity field as given in the earlier equations. The energy balance equation describing the latent heat release and interface change [Eq. (16)] is directly integrated within the context of weighted residuals,

$$\left(\int_\Omega \theta\,\hat{n}\cdot\nabla\theta^T\,\mathrm{d}V\right)\boldsymbol{T} - \left[\int_\Omega \left(\frac{k_{\text{cry}}}{k}\right)\theta\hat{n}\cdot\nabla\theta^T\,\mathrm{d}V\right]\boldsymbol{T}_{\text{cry}} = -\int_{\partial\Omega} q_T^*\theta\,\mathrm{d}S \tag{19}$$

This is applied as a surface energy source to the total thermal energy balance equation. The numerical implementation is similar to that used for a two-dimensional model,[18] except that one additional dimension needs to be considered. As with any other moving boundary algorithms, our interface tracking method uses an iterative procedure, by which the energy balance equation along the interface is applied as a surface source and the interface position coordinates searched based on each converged field calculations. The updated interface positions are then fed back to the field calculations until both the interface position coordinates and field variables are converged within a preset criterion, which is set at 1×10^{-4} (relative error) for the results to be presented.

IV. Results and Discussion

The full three-dimensional transient finite element model already described permits the prediction of both steady and transient fluid flow, heat and mass transfer, along with the solid–liquid interface morphology in single crystal growth systems under both terrestrial and microgravity conditions with and without applied magnetic fields. Extensive numerical simulations were carried out using the three-dimensional model. For the results to be presented, the final mesh used 8832 8-node brick elements with the increasing mesh distribution near the liquid–solid interfaces. The mesh is selected based on the mesh independence studies, as discussed in previous studies.[14,18] The thermophysical properties and geometric dimensions are given in Table 1. Numerical simulations used both synthesized and real g-jitter data, and a selection of results is presented.

A. Steady-State Microgravity Condition

The steady microgravity level of $10^{-6}\,g_0$ represents perhaps the best possible condition that can be achieved for the space growth

Table 1 Parameters used for calculations

Parameter	Value	Parameter	Value
	Physics properties		
T_{m0}	544 K	g_0	9.8 ms^{-2}
ρ_0	10,070 $\text{kg}\cdot\text{m}^{-3}$	H	5.25×10^4 $\text{J}\cdot\text{kg}^{-1}$
C_p	144.87 $\text{J}\cdot\text{kg}^{-1}\,\text{K}^{-1}$	k	12.4 $\text{W}\cdot\text{m}^{-1}\,\text{K}^{-1}$
ν	1.837×10^{-7} $\text{m}^2\cdot\text{s}^{-1}$	k_{cry}	6.5 $\text{W}\cdot\text{m}^{-1}\,\text{K}^{-1}$
D	2.7×10^{-9} $\text{m}^2\,\text{s}^{-1}$	k_{amp}	2.01 $\text{W}\cdot\text{m}^{-1}\,\text{K}^{-1}$
C_0	1 at.%	κ	8.5×10^{-6} $\text{m}^2\cdot\text{s}^{-1}$
β_T	1.25×10^{-4} K^{-1}	κ_{cry}	4.5×10^{-6} $\text{m}^2\cdot\text{s}^{-1}$
β_C	0.3049 (volume fraction)$^{-1}$	κ_{amp}	8.7×10^{-7} $\text{m}^2\cdot\text{s}^{-1}$
k_0	0.29 at.%/at.%	ε_{amp}	0.8
m	2.32 K/at.%		
	System parameters		
W_i	6.0×10^{-3} m	$\mathrm{d}T/\mathrm{d}x$	2.0×10^4 $\text{K}\cdot\text{m}^{-1}$
W_o	1.0×10^{-2} m	T_h	973 K
L	4.2×10^{-2} m	T_c	323 K
L_h	4.95×10^{-3} m	V_p	-3.34×10^{-6} ms^{-1}
L_c	4.95×10^{-3} m	B_0	0.5 T
L_g	3.21×10^{-3} m		
	Scale parameters		
U_0	6.12×10^{-5} ms^{-1}	R_0	3×10^{-3} m
ΔT	650 K	t_0	49.0 s
	Nondimensional parameters		
Pr	0.0215	Ha	38.7
Sc	68.0	Ra	0.01859
Gr_T	6.37×10^5	T_m	0.34
Gr_S	1.957×10^4	V_p	−0.055
Ste	0.558	T_c^*	0.497

of single crystals. Flight experiments show that this condition is obtained during a portion of space flight duration, and disruption occurs when g-jitter sets in. To study the g-jitter effects, an initial condition is required to start the transient calculations. In the present investigation, it is chosen to be results obtained for the melt flow and solidification under this steady-state microgravity condition. The steady-state solutions were obtained by setting all $\boldsymbol{M}$ terms (mass matrices) in Eq. (19) to zero and by assuming the gravity to be oriented in the direction perpendicular to the temperature gradient, for example, in the y direction. This arrangement represents the worst-case scenario for a steady-state microgravity condition. The computed results show that as in the two-dimensional case, the three-dimensional thermal field is primarily due to conduction with both steady and transient g-jitter forces, which is attributed that the Prandtl number Pr is small for the system being considered. Consequently, the thermal field is neglected in subsequent discussions. The flowfield is nearly dominated by the crystal pulling velocity because the double diffusive convection induced by the microgravity is weak. For the present system, the maximum velocity is 5.712×10^{-2}, which is slightly higher than the crystal pulling velocity 5.5×10^{-2}.

With such an approximate plug flow, the interface morphology is nearly axisymmetric and slightly concave into the crystal (Fig. 3). In Fig. 3, the calculations used the steady microgravity condition and the two-dimensional case refers to the results obtained using the two-dimensional model with the same conditions and the same solute dependent melting temperature. In Figs. 3 and 4, the results of

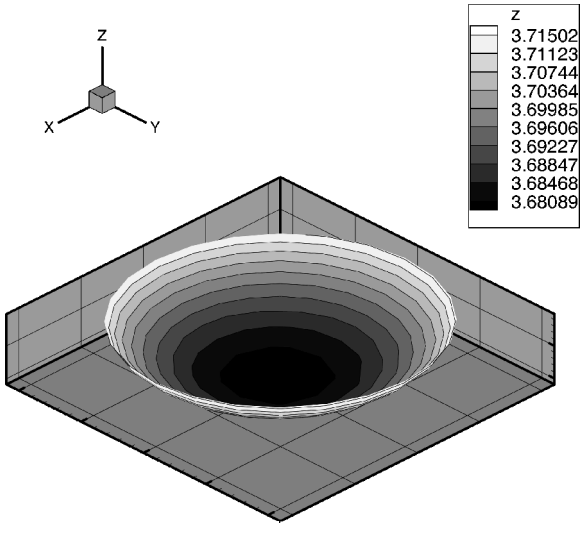

Fig. 3a Three-dimensional view of the interface shape with solute-dependent melting temperature.

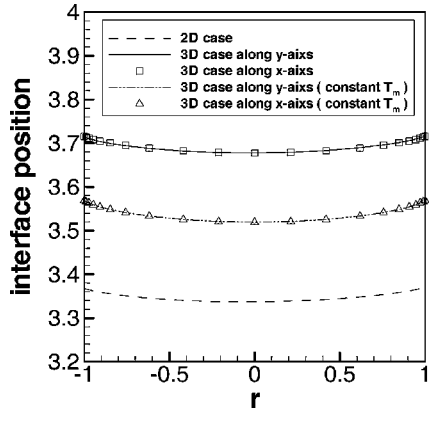

Fig. 3b Comparison of interface positions along the x and y axes without and with the dependency of melting temperature on concentration being accounted for.

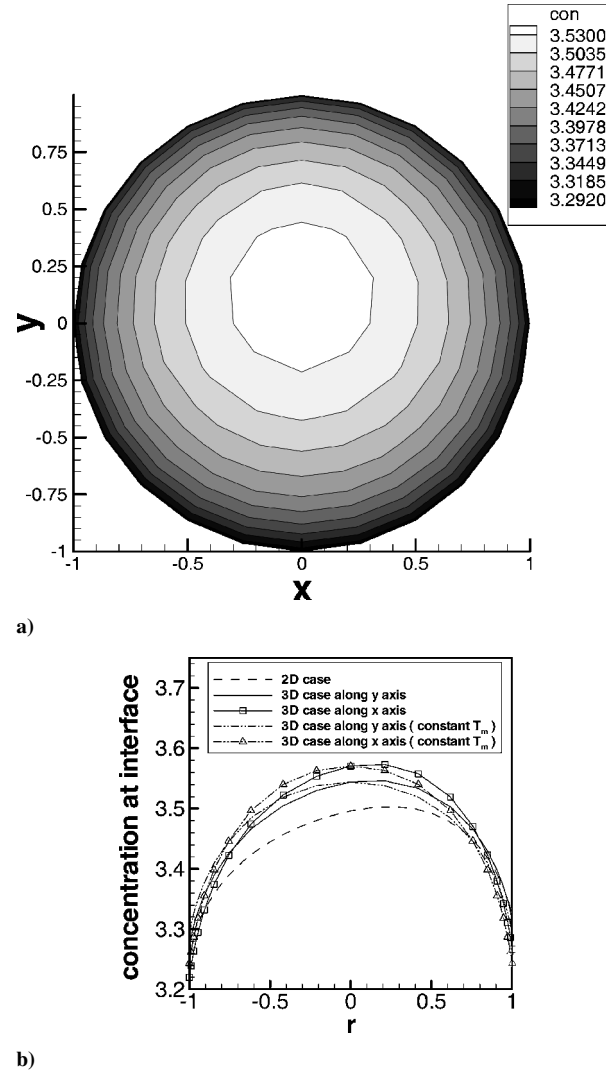

Fig. 4 Solute concentration distribution at a) interface and b) along x and y axes.

the three-dimensional model with T_m taken to be independent of concentration and of the earlier two-dimensional model are also plotted for comparison. In Fig. 4, the parameters used for calculations are the same as in Fig. 4. Clearly, the two-dimensional model predicts a very similar interface shape to that by the three-dimensional model, which is slightly concaved into the crystal. With this concave interface and an absence of convection, the solute concentration at the interface would be axisymmetric with a maximum at the center of the interface.[23] The effect of the weak double diffusive convection induced by microgravity is to distort the axisymmetric solute distribution (Fig. 4). Measured by $(C_{\max} - C_{\min})/C_{\text{av}}$ at the growth interface, the solute distribution has a nonuniformity of 8.03%. The effect of the solute concentration-dependent melting temperature on the solidification system performance is also evaluated in Fig. 3b. It is seen that in the case of constant melting temperature, the interface has a noticeable shift toward the cold end, and the solute concentration distribution at the interface has a larger nonuniformity of 10.5% (Fig. 4b). These results reveal that even under a steady-state microgravity condition, the axisymmetric assumption for the solute concentration distribution may not be strictly maintained for the present three-dimensional system, and thus, the solute dependency of melting temperature must be accounted for to predict the solidification phenomena accurately.

B. Single Frequency g-Jitter Data

The real g-jitter perturbation is random both spatially and temporally. In some cases, to help analyses, the real g-jitter data can be

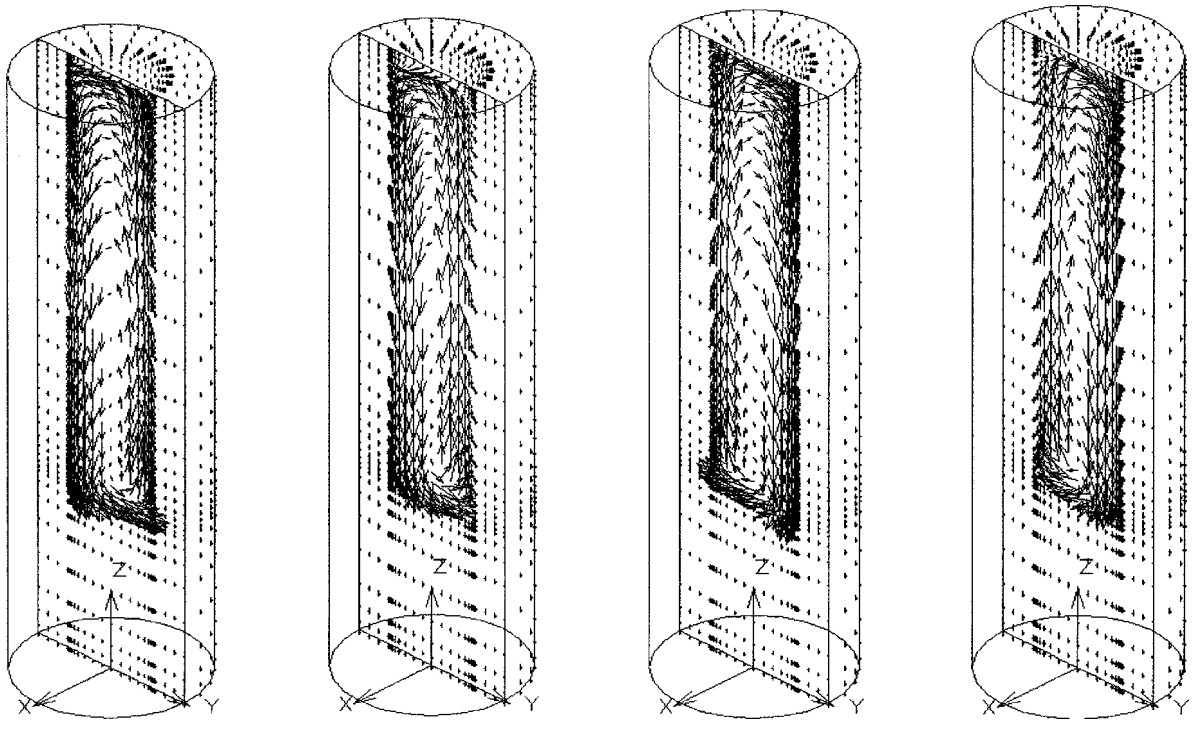

Fig. 5 Time development of single-frequency *g*-jitter induced velocity field in the *y*–*z* plane over one time period in the absence of a magnetic field: a) $t_1 = 3.927$, $U_{max} = 0.7725$; b) $t_2 = 3.978$, $U_{max} = 0.6857$; c) $t_3 = 4.029$, $U_{max} = 0.7725$; and d) $t_4 = 4.080$, $U_{max} = 0.6857$.

represented by a synthesized series of single-frequency *g*-jitter data as follows:

$$\boldsymbol{g}(t) = \sum_{n=1}^{N} \boldsymbol{g}_n \sin(2\pi\omega_n t) \tag{20}$$

Moreover, space-flight experiments with single crystal growth suggest that only the large magnitude *g*-jitter components in a low-frequency range produce the most deleterious effects on the crystal quality. Thus, the synthetic single frequency *g*-jitter, $g(t) = 10^{-3}\sin(0.2\pi t)$, oriented in the y direction is adopted in the present study. Although unrealistic with a space environment, the single-component *g*-jitter force is useful for developing a fundamental understanding of physics governing the effects of gravity perturbation on convection and solidification phenomena. The computed three-dimensional results for a single-frequency *g*-jitter force illustrate that the melt flow changes with time when *g*-jitter sets in and finally evolves into a quasi-steady-steady-state characterized by a time-harmonic motion, as appear in Figs. 5 and 6. This is similar to that predicted by a two-dimensional model. Examination of Figs. 5 and 6 shows that the *g*-jitter induced convection loop covers the entire melt region and sweeps along the solid–liquid interface. In the y–z (or $x = 0$) plane (Fig. 5), the convection loop oscillates and reverses its rotating direction at approximately the same frequency of the applied *g*-jitter. The flow pattern in the x–z (or $y = 0$) plane (Fig. 6) is more complex and reveals the three-dimensional nature of the melt flow. However, the oscillation of the convective loop still is evident in the regions near the inlet and solidification interface. Additional numerical simulations reveal that the intensity of the melt flow increases with the amplitude of the *g*-jitter driving force, which is consistent with the two-dimensional model predictions.

For practical applications, the u and v components of the melt flow velocity and the solute concentration in the region near the growth interface are crucial because of their direct implication to crystal quality. The evolution of these field quantities at two points in the melt near the growth front is shown in Fig. 7, where the two selected points are in the x–z plane and y–z plane, respectively. Calulations used the single-frequency modulation. It is seen from Fig. 7 that the velocity components oscillate with time at the same frequency of the driving *g*-jitter force when the quasi-steady state is reached and so does the solute concentration oscillation. These characteristics agree well with those predicted by the two-dimensional model[18] qualitatively. Also note that, at the point in the y–z plane, the x-direction velocity component u is nearly zero because of its location and the orientation of the *g*-jitter force. The effects of the three-dimensional melt flow on the interface morphology and the solute concentration distribution at the interface over a period are shown in Figs. 8a and 8b. In Fig. 8, calculations used the single-frequency modulation. Here the interface position along the x axis remains essentially unchanged with time, but that along the y axis oscillates time harmonically. Moreover, the interface shape is not axisymmetric, a manifestation of the convective flow effects. The solute concentration distribution along the x axis and the y axis is approximately constant, but the difference between them is larger compared with that for the initial steady case. The evolution of the concentration nonuniformity at the interface measured by $[C(t)_{max} - C(t)_{min}]/C(t)_{av}$ is shown in Fig. 9. Clearly the concentration nonuniformity is exacerbated by the *g*-jitter induced melt flow, which is deleterious for the crystal quality. Calulations in Fig. 9 also used the single-frequency modulation.

With the three-dimensional model, the effects of the interface shape on the concentration distribution at the interface can also be studied. The computed results indicate that, for a flat interface case, the maximum velocities of the flowfield over a time period are nearly identical to those of the curved interface case. However, the concentration distributions at the interface (Fig. 8d) are much more uniform compared with the curve interface case, which result in a much smaller concentration nonuniformity at the interface, as shown in Fig. 9.

One of the important findings obtained from the previous study[18] is that a dc magnetic field is useful in suppressing the deleterious convection effects associated with *g*-jitter. This is also corroborated by the results from extensive three-dimensional simulations, which were made with various magnetic field configurations. In summary,

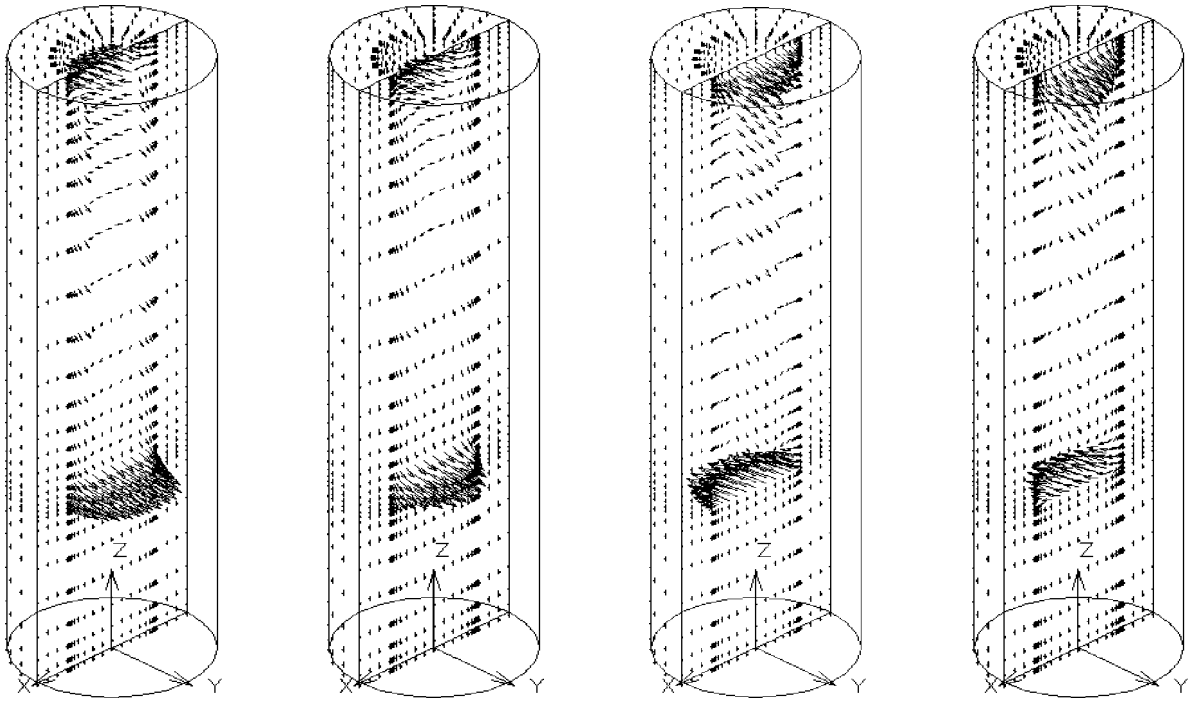

Fig. 6 Evolution of single-frequency *g*-jitter induced velocity field in the *x*–*z* plane over one time period without a magnetic field: a) $t_1 = 3.927$, $U_{max} = 0.7725$; b) $t_2 = 3.978$, $U_{max} = 0.6857$; c) $t_3 = 4.029$, $U_{max} = 0.7725$; and d) $t_4 = 4.080$, $U_{max} = 0.6857$.

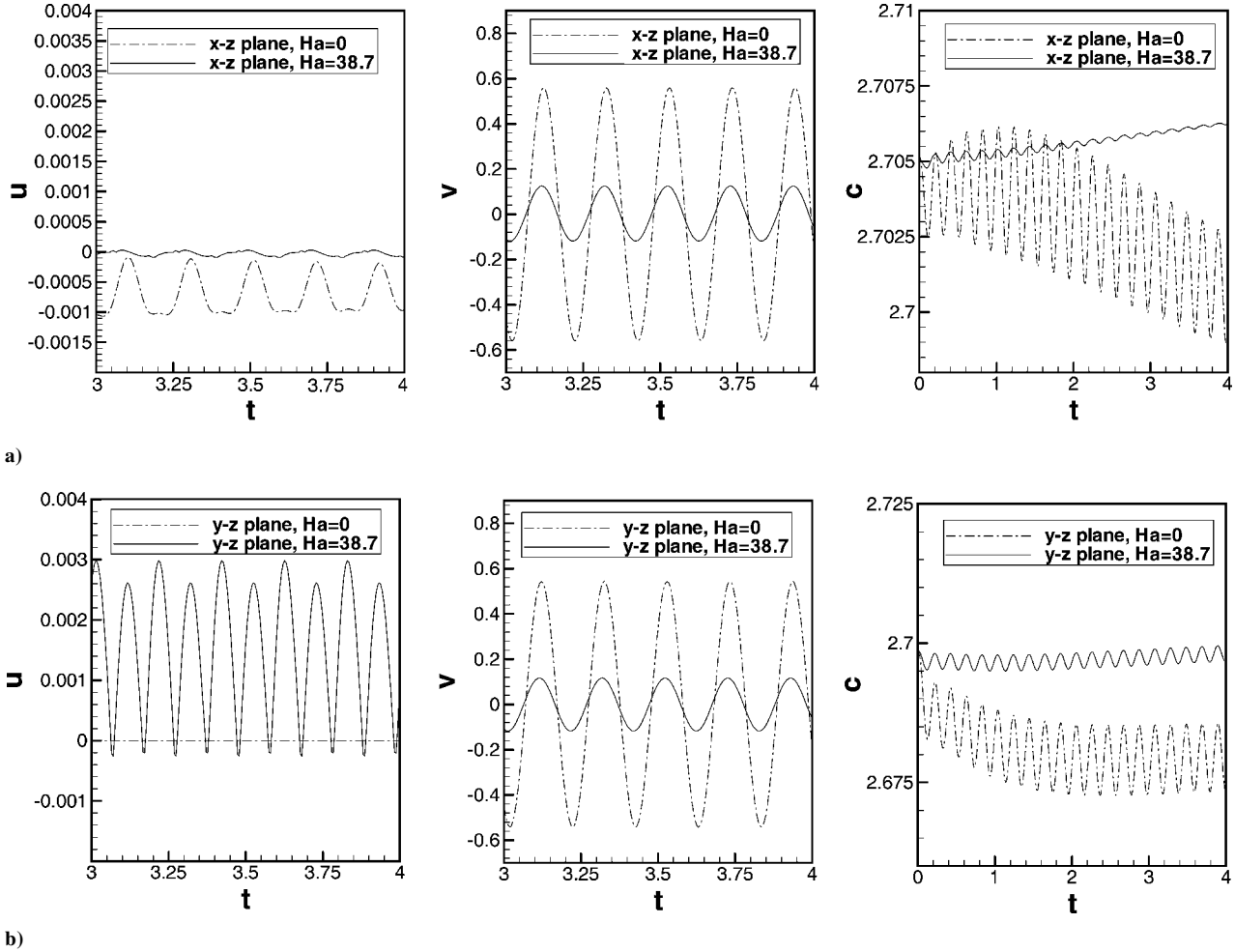

Fig. 7 Transient development of velocity components *u* and *v* and solute concentration *c* with and without a magnetic field a) at $x = -0.214$, $y = 0$, and $z = 3.786$ in *x*–*z* plane and b) at $x = 0$, $y = -0.214$, and $z = 3.786$ in *y*–*z* plane.

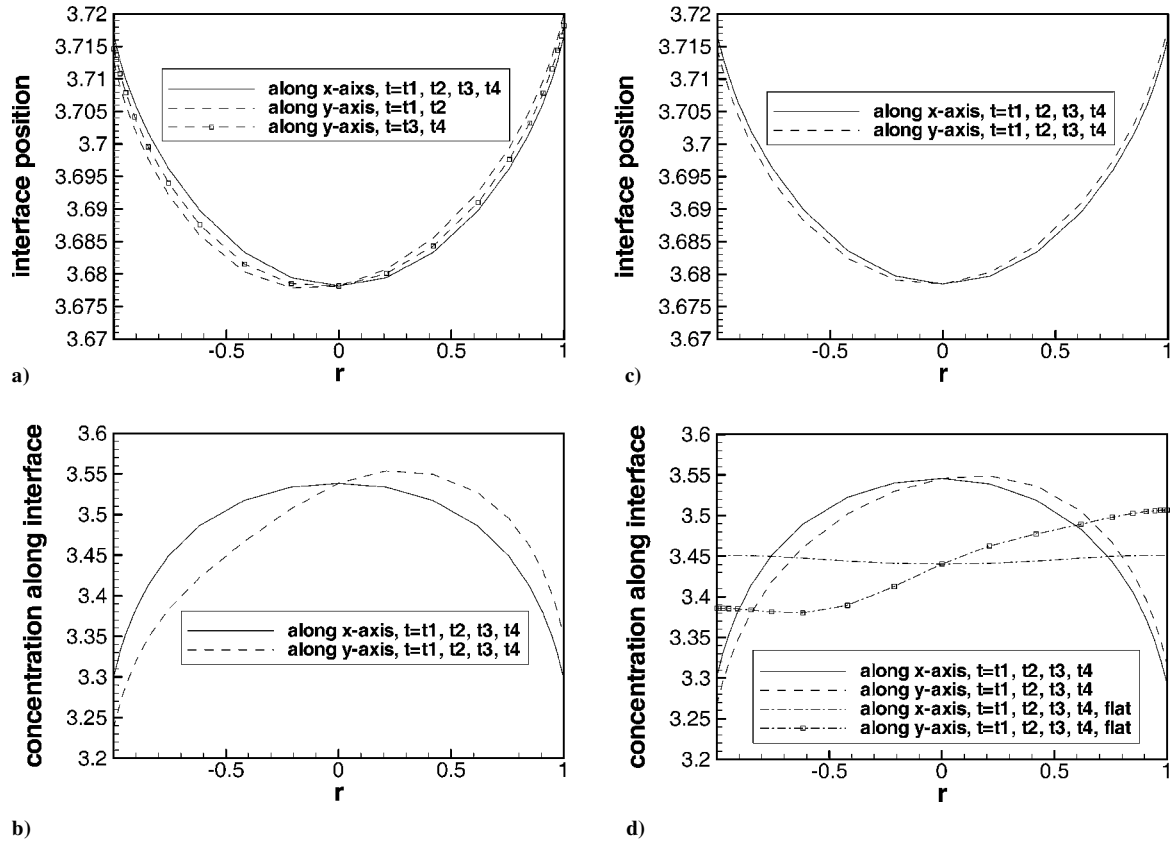

Fig. 8 Interface position and the solute concentration distribution at interface along the x and y axes without [a) and b)] and with [b) and c)] an external magnetic field over one time period: $t_1 = 3.927, t_2 = 3.978, t_3 = 4.029$, and $t_4 = 4.080$.

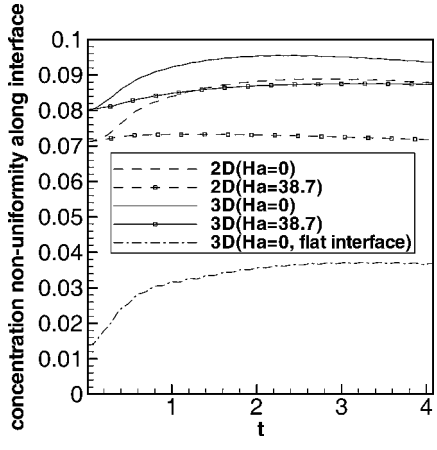

Fig. 9 Evolution of solute concentration nonuniformity at the interface measured by $[C(t)_{max} - C(t)_{min}]/C(t)_{av}$ for two- and three-dimensional cases with and without a magnetic field.

these three-dimensional results reveal that an applied magnetic field is effective in reducing the magnitude of the convective flows, but it does not affect the main convection loop, which oscillates in time with the same frequency as the driving g-jitter force. The applied field, however, does affect the phase angle of the velocity components. The reduced convection in the liquid pool in turn helps to produce a more uniform distribution of the concentration at the solid–liquid interface, although it still oscillates time harmonically. These findings are clearly displayed in Figs. 7–9, which plot the evolution of velocity components and concentration distributions as well as the interface positions in the presence of a magnetic field applied in the z direction. Besides these known effects, an applied magnetic field also leads to a more complex three-dimensional flow, as discussed next.

C. Two-Dimensional Versus Three-Dimensional Models

At this point, it may be worthwhile to make an excursion to assess the applicability and limitations of the two-dimensional model developed earlier.[18] The snapshots (at $t = 4.080$) of the flowfields calculated by the two-dimensional and three-dimensional models are shown in Fig. 10. In Fig. 10, the results are plotted at $t_4 = 4.080$ and calculations used the single-frequency g-jitter modulation. Comparison of these results shows that the flow patterns in the y–z plane of the three-dimensional model in which the gravity force acts qualitatively agree with those obtained from the two-dimensional model with and without applied magnetic fields. This conclusion also holds true for the temperature and solute distributions in the y–z plane, and the evolution of the solute concentration nonuniformity at the interface (Fig. 9). Similar conclusions are also reached from both two- and three-dimensional numerical simulations for other conditions, such as real g-jitter data, insofar as the g-jitter force is confined in a plane cutting through the vertical axis. From these results, one may conclude that a two-dimensional model provides a reasonably good approximation of the three-dimensional flow and scalar transport in the y–z plane in which the gravity force acts. Perhaps, this may be the best result one can hope for, in light of the intrinsic assumptions associated with a two-dimensional model. In the other planes, however, the results from the three-dimensional model may differ significantly from the two-dimensional model. Also, for the case being considered, the three-dimensional nonlinear interactions result in a subharmonic, that is, frequency doubling, variation of u and w components in the y–z plane in the presence of a magnetic field (Fig. 7), though its magnitude is small in comparison with the v-component. Further difference occurs when all three components of g-jitter perturbations are considered. Thus, although a two-dimensional model can be a reasonably useful tool for a fundamental understanding, a three-dimensional model is required for a realistic description of full three-dimensional g-jitter effects on transport phenomena and solidification in a space environment.

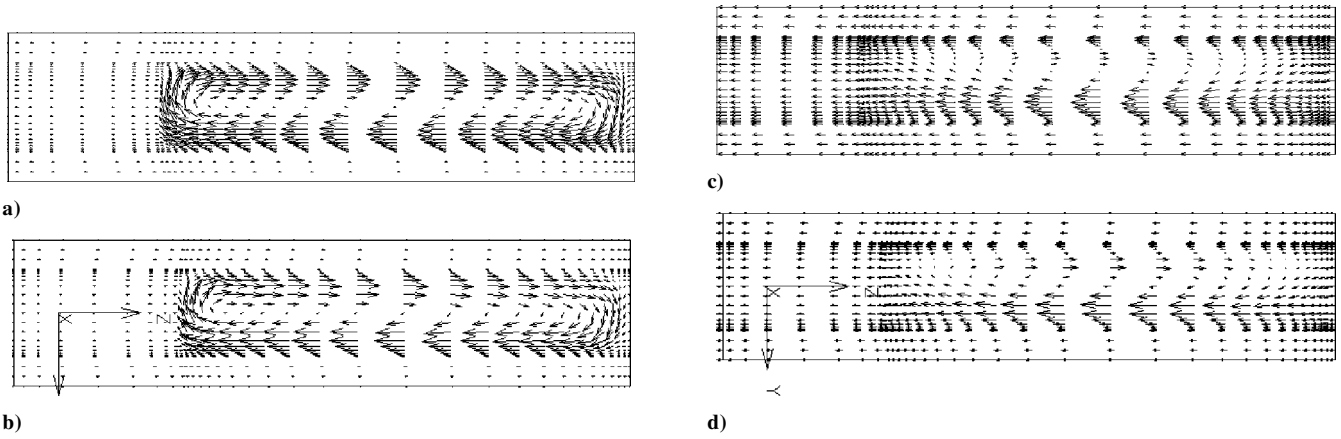

Fig. 10 Comparison of three-dimensional and two-dimensional flow patterns with and without an applied magnetic field: a) three-dimensional velocity profile in the *y*–*z* plane without and b) with an applied field and c) two-dimensional flow profile without and d) with an applied field.

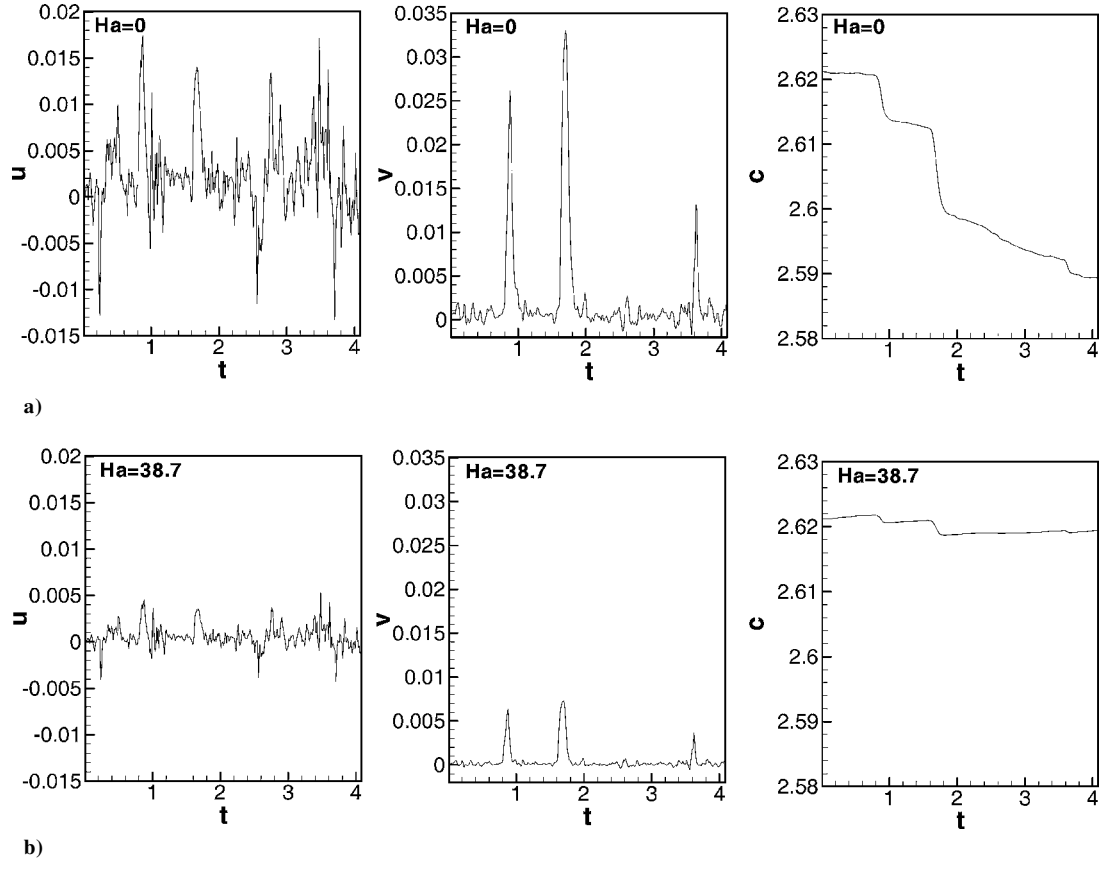

Fig. 11 Evolution of velocity components *u* and *v* and solute concentration *c* at $x = 0$, $y = -0.757$, and $z = 3.800$ under the real *g*-jitter perturbations: a) without and b) with magnetic field.

D. Real *g*-Jitter Data

As stated earlier, the real *g*-jitter perturbation is random both spatially and temporally; consequently, the melt flows in the current system are bound to be complex. With the three-dimensional model, numerical simulations were conducted using the *g*-jitter data taken by an onboard accelerometer during a space flight, as shown in Fig. 2. The evolution of velocity components u and v and solute concentration c at the points near the growth front in the melt is shown in Figs. 11 and 12, again the two selected points being in the y–z (Fig. 11) and x–z (Fig. 12) planes. Here, the *g*-jitter induced convection cell varies irregularly with time to reflect the nature of the *g*-jitter driving forces. The spikes of velocities emerge in response to the *g*-jitter perturbations during the space flight, which in turn cause irregular changes in solute distribution. These irregularities in velocity and concentration are responsible for inconsistent qualities of crystals grown in space. Analysis of the flow patterns at the time when the highest velocity spike emerges (Figs. 11 and 12) shows that the induced convection cell appears to be strong and covers the entire melt region ($U_{\max} = 0.2607$). The flow pattern is three dimensional and is consistent with the random nature of *g*-jitter.

As in the single-frequency case, external magnetic fields also are found to be effective in damping out the irregular *g*-jitter induced convection effects. This is confirmed by three-dimensional numerical simulations for various field configurations, and one of these calculations ($Ha = 38.7$, $B_0 = 0.5$ T) is plotted in Figs. 11 and 12, along with those with and without the applied magnetic field. Detailed analysis further shows that an applied magnetic field is

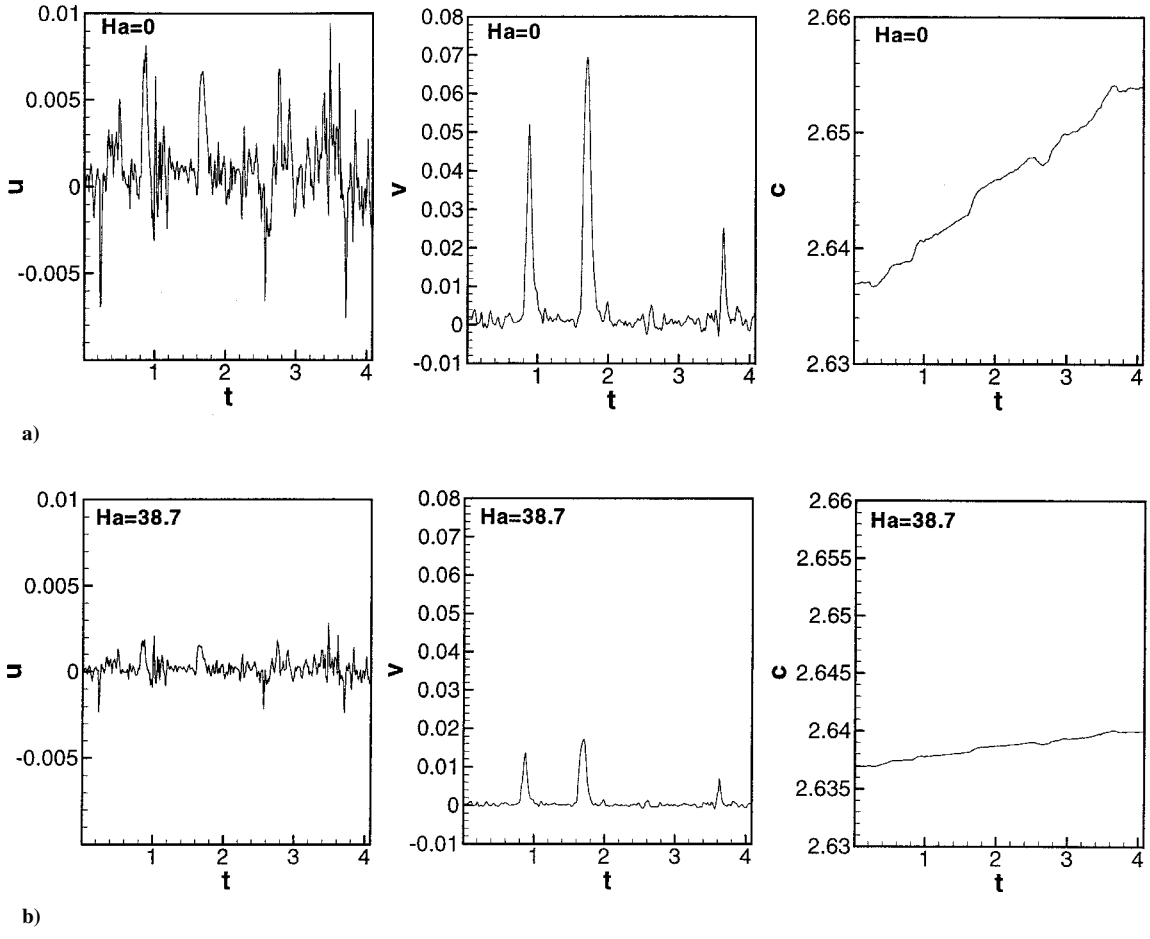

Fig. 12 Evolution of velocity components u and v and solute concentration c at $x = 0.757, y = 0$, and $z = 3.800$ under the real g-jitter: a) without and b) with magnetic field.

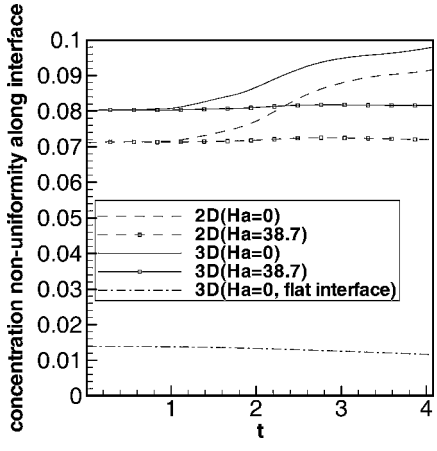

Fig. 13 Evolution of solute concentration nonuniformity at the interface measured by $[C(t)_{max} - C(t)_{min}]/C(t)_{av}$ for the two- and three-dimensional cases with and without magnetic field under the real g-jitter.

more effective in damping out the large-amplitude velocity spikes, which is consistent the basic principle of magnetohydrodynamics. Inspection of Figs. 11 and 12 illustrates that, with the applied magnetic field, the velocity spikes are substantially reduced ($U_{max} = 0.1671$ with $Ha = 38.7$ compared with $U_{max} = 0.2607$ with $Ha = 0$), whereby the solute variations are subdued. Additional three-dimensional simulations suggest that an appropriate magnetic field strength may be selected to suppress the convective flows below a preset threshold value so that a diffusion controlled growth mechanism becomes possible with a combined action of magnetic field and microgravity.

The transient development of the concentration nonuniformity at the interface under the influence of real g-jitter is shown in Fig. 13 for the two- and three-dimensional cases with and without magnetic damping. It transpires that real g-jitter perturbations strongly perturb the solute concentration distribution near the interface and greatly increase the concentration nonuniformity. A reduction of the oscillating melt flow by magnetic fields greatly improves the concentration uniformity at the solidification interface, which is evident in the results plotted in Fig. 13. Inspection of Fig. 13 also suggests that the solute concentration nonuniformity profiles predicted by the two- and three-dimensional models agree well qualitatively with or without an applied magnetic field. For comparison, the results obtained by neglecting solidification with an assumed flat interface are also shown in Fig. 13, where it is seen that a flat interface model appears to underpredict the solute concentration uniformity at the interface.

V. Conclusions

This paper has presented a three-dimensional finite element model for the melt growth of single crystals in space. The model is developed based on the deforming finite element methodology to predict the phenomena of full three-dimensional steady-state and transient melt convective flows, heat transfer and solute distribution, and solid–liquid interface morphology associated with single crystal growth in microgravity with and without an applied magnetic field. Computed results show that the g-jitter induced flow is time dependent and exhibits a complex three-dimensional pattern that in turn produces detrimental effects on the crystal growth. An applied magnetic field of appropriate strength, superimposed on the microgravity, can provide a viable means to suppress or eliminate the deleterious effects resulting from the g-jitter disturbance. Full

three-dimensional simulations demonstrate that a two-dimensional model is useful in providing some essential features of g-jitter induced flows and solidification behavior when a g-jitter force is confined in a plane. However, a three-dimensional model is required to fully appreciate the complex spatial flow structure when all three components of g-jitter are operative, as in a space flight. Also the concentration effects on interface morphology need to be considered for a more quantitatively accurate prediction of solidification behavior.

Acknowledgment

The authors are grateful for the financial support of this work by the NASA Microgravity Science and Application Division (Grant NAG8-1693).

References

[1]Alexander, J. I. D., "Low-gravity Experiment Sensitivity to Residual Acceleration: A Review," *Microgravity Science and Technology*, Vol. 2, No. 1, 1994, pp. 131–135.

[2]Alexander, J. I. D., Quazzani, J., and Rosenberger, F., "Analysis of the Low Gravity Tolerance of the Bridgman–Stockbarger Crystal Growth I: Steady and Impulse Accelerations," *Journal of Crystal Growth*, Vol. 97, No. 2, 1989, pp. 285–302.

[3]Alexander, J. I. D., Amiroudine, S., Quazzani, J., and Rosenberger, F., "Analysis of the Low Gravity Tolerance of the Bridgman-Stockbarger Crystal Growth II: Transient and Periodic Accelerations," *Journal of Crystal Growth*, Vol. 113, Nos. 1–2, 1991, pp. 21–38.

[4]Schneider, S., and Straub, J., "Influence of the Prandtl Number on Laminar Natural Convection in a Cylinder Caused by G-jitter," *Journal of Crystal Growth*, Vol. 97, No. 1, 1989, pp. 235–242.

[5]Zhang, W., Casademunt, J., and Venals, J., "Study of Parametric Oscillator Driven by Narrow-band Noise to Model the Response of a Fluid Surface to Time-dependent Acceleration," *Physics of Fluids A: Fluid Dynamics*, Vol. 5, No. 12, 1993, pp. 3147–3152.

[6]Wheeler, A. A., Mcfadden, G. B., Murray, B. T., and Coriell, S. R., "Convection Stability in Rayleigh–Benard and Directional Solidification Problems: High Frequency Gravity Modulation," *Physics of Fluids A: Fluid Dynamics*, Vol. 3, No. 8, 1991, pp. 2847–2853.

[7]Benjapiyaporn, C., Timchenko, V., Leonardi, E., De Vahl Davis, G., and de Groh, H. C., III, "Effects of Space Environment on Flow and Concentration during Directional Solidification," NASA TM 209293, 2000.

[8]Timchenko, V., Chen, P. Y. P., Leonardi, E., De Vahl Davis, G., and Abbaschian, R., "A Computational Study of Transient Plane Front Solidification of Alloys in a Bridgman Apparatus under Microgravity Conditions," *International Journal of Heat and Mass Transfer*, Vol. 43, No. 6, 2000, pp. 963–980.

[9]Series, R. W., and Hurle, D. T. J., "The Use of Magnetic Field in Semiconductor Crystal Growth," *Journal of Crystal Growth*, Vol. 113, Nos. 1–2, 1991, pp. 305–328.

[10]Ma, N., and Walker, J. S., "Magnetic Damping of Buoyant Convection during Semiconductor Crystal Growth in Microgravity: Spikes on Residual Acceleration," *Physics of Fluids*, Vol. 8, No. 4, 1996, pp. 944–949.

[11]Baumgartl, J., and Muller, G., "The Use of Magnetic Fields for Damping the Action of Gravity Fluctuations (G-jitter) During Crystal Growth under Microgravity," *Journal of Crystal Growth*, Vol. 169, No. 3, 1996, pp. 582–586.

[12]Pan, B., and Li, B. Q., "Effects of Magnetic Field on Oscillating Mixed Convection," *International Journal of Heat and Mass Transfer*, Vol. 41, No. 17, 1998, pp. 2705–2710.

[13]Shang, D. Y., Li, B. Q., and de Groh, H. C., III, "Magnetic Damping of G-jitter Driven Flows: 3-D Calculations," *Journal of Japanese Society of Microgravity Application*, Vol. 15, Supplement 2, 1998, pp. 108–113.

[14]Handa, J., Zhang, X., Li, B. Q., and de Groh, H. C., "A 3-d Model for Magnetic Damping of G-jitter Induced Convection and Solutal Transport in a Simplified Bridgmann Configuration," *Proceedings of the ASME Heat Transfer Division*, American Society of Mechanical Engineers, New York, 2001, pp. 1–18.

[15]Li, B.Q., "Stability of Modulated-Gravity-Induced Thermal Convection in a Magnetic Field," *Physical Review E: Statistical Physics, Plasmas, Fluids, and Related Interdisciplinary Topics*, Vol. 63, No. 41, 2001, pp. 041508-1–041508-9.

[16]Pan, B., Shang, D. Y., Li, B. Q., and de Groh, H. C., III, "Magnetic Field Effects on g-Jitter Induced Flow and Solute Transport," *International Journal of Heat and Mass Transfer*, Vol. 45, No. 1, 2002, pp. 125–144.

[17]Shu, Y., Li, B. Q., and de Groh, H. C., "Magnetic Damping of G-jitter Induced Double Diffusive Convection in Microgravity," *Numerical Heat Transfer A: Applications*, Vol. 42, No. 4, 2002, pp. 345–364.

[18]Li, K., Li, B. Q., and de Groh, H. C., "Numerical Analysis of Double Diffusive Convection and Solidification Under G-Jitter and Magnetic Fields," *Journal of Thermophysics and Heat Transfer*, Vol. 17, No. 2, 2003, pp. 199–209.

[19]Li, B. Q., and He, R., "Computational Modeling of Electrodynamic and Transport Phenomena under Terrestrial and Microgravity Conditions," *International Journal of Applied Electromagnetics and Mechanics*, Vol. 14, 2002, pp. 459–466.

[20]Yao, M. W., Raman, R., and de Groh, H. C., III, "Numerical Simulation of Heat and Mass Transport During Space Crystal Growth with MEPHISTO," NASA TM 107015, July 1995.

[21]Li, B. Q., "G-jitter Induced Flows in A Transverse Magnetic Field," *International Journal of Heat and Mass Transfer*, Vol. 39, No. 14, 1996, pp. 2853–2860.

[22]Song, S. P., and Li, B. Q., "A Hybrid Boundary/Finite Element Method for Simulating Viscous Flows and Shapes of Droplets in Electric Fields," *International Journal of Computational Fluid Dynamics*, Vol. 15, No. 2, 2002, pp. 293–308.

[23]Coriell, S. R., and Sekerka, R. F., "Lateral Solute Segregation During Unidirectional Solidification of a Binary Alloy with a Curved Solid–Liquid Interface: II. Large Departures from Planarity," *Journal of Crystal Growth*, Vol. 54, No. 2, 1981, pp. 167–175.